E JOURNAL

Stereo-based image processing for spatter detection in PBF-LB/M of Ti-6Al-4V

Nicole Emminghaus[1] · Tim Klügel[1] · Jörg Hermsdorf[1] · Stefan Kaierle[1,2]

[1] Laser Zentrum Hannover e. V., Hollerithallee 8, 30419 Hannover, Germany
[2] Leibniz Universität Hannover, Institut für Transport- und Automatisierungstechnik, An der Universität 2, 30823 Garbsen, Germany

https://doi.org/10.58134/fh-aachen-rte_2024_010

Abstract
Spattering is an inevitable by-product of the laser-based powder bed fusion of metals (PBF-LB/M) that can lead to deterioration of the part properties as well as degradation of the unmolten powder. To understand the spattering phenomenon and develop effective countermeasures, a monitoring system is required that can record and process the 3-dimensional movement behavior of the spatter particles. In this work, a stereo-vision camera setup with subsequent image analysis is presented for the PBF-LB/M of the titanium alloy Ti-6Al-4V. The influence of the process parameters laser power and scanning speed on spatter generation is also investigated experimentally. Spatter speeds between 13.01 m/s and 35.77 m/s were determined. The results show a correlation between spatter generation and volume energy density. An increase in spatter amount was observed when the laser power was increased, or the scanning speed was reduced. Further, as the volume energy density increased, the spatter velocity also increased, and the spatter size decreased. In addition to the process parameters, the influence of the gas flow on the spatter trajectory is considered. The gas flow in the process chamber causes a change in the direction of the spatter trajectories as they leave the process zone. Spatters already moving parallel to the gas flow are accelerated. This work highlights the importance of a 3-dimensional monitoring of the spattering to develop a deeper understanding of the underlying mechanisms and shows that by adjusting the process parameters the process can be significantly influenced.

Keywords Additive Manufacturing · Ti-6Al-4V · PBF-LB/M · spatter · melt pool · process monitoring

1. Introduction and motivation

The laser-based powder bed fusion of metals (PBF-LB/M) is known for its ability to generate complex parts with intricate shapes and its economic suitability for small quantities and individual parts. Another often mentioned advantage is the high degree of material utilization [1,2]. However, this advantage only really becomes apparent if the unmelted powder can be permanently reused. Yet, it has been shown that the more the powder is recycled, the more it degrades [3,4]. By Raza et al. spatter formation and the resulting accumulation of oxidized particles is cited as the main reason for this [5,6]. Spatter particles can be of various shapes and sizes. Large agglomerate particles can be sieved out before the next use. In contrast, small particles, that might be severely oxidized can't be filtered out and can lead to mechanical or chemical flaws in the final parts [7]. Furthermore, spattering can degrade the surface quality of the built parts and by this increase the likelihood of lack-of-fusion defects [8,9]. Consequently, the formation of spatters and their deposition in the process zone are strongly linked to the resulting part properties. To take effective countermeasures and therefore improve process stability and part quality it is fundamental to understand the spattering phenomenon and the influencing parameters in the PBF-LB/M process. To gain insights into the process zone, suitable monitoring techniques to detect and track the spatters are needed. According to Li et al. the suitable techniques for spatter detection include the use of visible-light high-speed cameras, X-ray video imaging, infrared video imaging and schlieren video imaging [10]. The use of visible-light high-speed cameras represents a cost-effective and easy-to-integrate solution provided that the installation is done in an off-axis setup. On-axis setups are able to monitor the meltpool in addition to the spatters and are used in various studies as given by the review work of Li et al. [10]. However, such a setup requires the integration into the optical path which is not possible for all machines. It also leads to a projection of the spatter trajectories onto

the viewing plane and therefore the inability to correctly determine the spatter velocities. An off-axial setup can be integrated at any angle to the side of the process zone. It is also able to observe the spatter ejection angles.
Using this type of setup, various works investigated the spatter and plume behavior using image acquisition rates between 2,000 and 20,000 fps [11–16]. Di Wang et al. demonstrated that the type of spattering, i. e. the ejection of droplet spatter from the meltpool and the ejection of entrained and heated powder particles, is determined by the energy input [11]. The energy input can be described by the volume energy density E_V according to equation 1:

$$E_V = \frac{P}{v \cdot h \cdot t} \qquad (1)$$

Andani et al. found that the underlying scanning speed *v* had a stronger influence on the spattering than the overall volume energy density [14], that also includes the laser power *P*, the hatch distance *h* and the layer thickness *t*.
A major disadvantage of spatter observation with a single camera, both coaxial and off-axial, is that the spatter movements are always projected onto the viewing plane. This results in a falsification of the spatter velocities and a three-dimensional characterization of the trajectories is not possible. A solution to this is the implementation of a stereo-camera setup as presented by Barrett et al. and Eschner et al. [17,18]. However, a detailed investigation of the influences on the spatter behavior using this type of monitoring has not been done so far. Therefore, this work aims to provide first experiments with different volume energy densities as well as different settings for laser power and scanning speed and different scan orientations with regard to the gas flow direction for a self-designed stereo-vision camera setup. For evaluation of the spatter trajectories a self-developed algorithm using the computer vision library OpenCV in Python was used.

2. Materials and methods

In the following, the used powder, the employed machines as well as the monitoring system are described. Detailed information about the stereo-camera-based spatter detection is given and the chosen experimental design is illustrated.

2.1. Material

In order to test the stereo-camera system and examine the process influences, Ti-6Al-4V powder was processed. The gas atomized powder has a mainly spherical morphology, as it can be seen in the SEM (scanning electron microscopy) image in Figure 1. It has a specified particle size range of 20-63 µm and was reused and sieved several times before the experiments. The Hall flowability (ASTM B213) was measured to be 30 s/50 g and the apparent density 2.38 g/cm³.

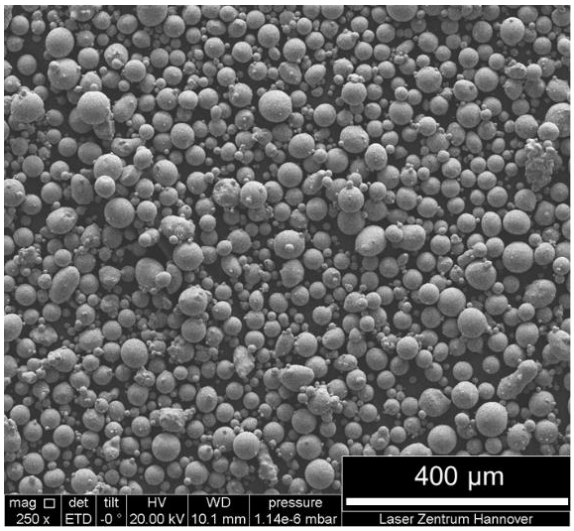

Figure 1: SEM image of the used Ti-6Al-4V powder

2.2. Experimental equipment

For the experiments, a laboratory machine was used. This machine is described in detail in [19] and was originally developed to conduct the PBF-LB/M process under an oxygen-free atmosphere, containing small amounts of monosilane. However, the process can also be carried out under conventional argon atmosphere with a residual oxygen content of 0.01 vol.-%. Within the machine a continuous wave Yb-fiberlaser (YLR-500-AC by IPG Laser GmbH, Germany) with a wavelength of 1070 nm and a maximum power of 500 W in combination with the scanner module AM-Module Next Gen by Raylase GmbH, Germany is used. For the process the minimum spot diameter of 38 µm is used.
Within the processing chamber the machine provides a continuous argon gas flow with a speed of 1.7 m/s above the powder bed to remove spatter and plume from the process zone. A round buildplate with a diameter of 100 mm as well as a rubber lip coater are integrated.

2.3. Stereo-camera system and image processing

To observe the process zone, the stereo-camera system is placed in front of a monitoring window. The cameras are installed slightly above the level of the powder bed and are able to record the entire buildplate. Figure 2 shows a schematic representation of the process chamber and the position of the stereo-camera system.

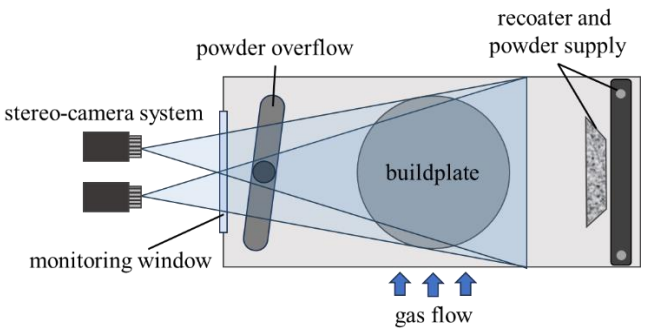

Figure 2: Schematic representation of the process chamber and position of the stereo-camera system

The implemented stereo-camera system consists of two individual high-speed cameras (MQ003MG-CM by XIMEA GmbH). With the dimensions of 26 mm x 26 mm x 24 mm and an image acquisition rate of 500 fps these cameras represent a small, easy-to-integrate and cost-effective (< 1000 €) solution for process monitoring in PBF-LB/M-machines that are often very limited regarding the available space. The cameras were combined with the lenses T3Z3510CS (Computar by CBC AMERICA LLC). Further technical information regarding the cameras and the chosen settings are given in Table 1.

Table 1: Technical camera information

Specification	**Value**
Frame rate	500 fps
Resolution	648 pixel x 488 pixel
Exposure time	1.5 ms
Acquisition time	20 s
Color	monochromatic
Sensor type	CMOS
Data transfer	USB 3.0

For image acquisition as well as subsequent image processing and spatter trajectory evaluation python scripts were developed using the computer vision library OpenCV.

The workflow for the use of the stereo-camera setup to determine the spatter trajectories consists of four subsequent steps that are realized as single programs: calibration, image acquisition, transformation into video format and trajectory analysis.
Calibration is used to determine the geometric arrangement of the cameras in relation to each other, which is required for triangulation. In addition, the calibration of the system serves to rectify captured images. First, the camera parameters, such as the focal length and the distortion factors, are determined for each camera individually. The stereo system is then calculated with the associated base length as well as the rotation matrix and translation vector. Using the determined parameters, rectification is then carried out and a calibration file with the corresponding parameters is created. For calibration purposes a checkerboard pattern with known size of the single squares can be moved inside the process chamber.
The camera manufacturer's API (XIMEA CamTool) is used to actually record the images. This allows to set the acquisition rate and exposure time, which offers fine-tuning to the respective process. After the images have been recorded, they are initially written to a buffer. When the buffer is completely full, recording ends and the images are saved on the computer. A multi-process is created in Python to read out the cameras, as this is the only way two tasks can be carried out at the same time.
The subsequent transformation of the images into video files reduces the required storage capacity and allows for easier data exchange. The last program for the determination of the spatter trajectories is divided into the spatter detection and the spatter tracking.
In the first step, the edges of each frame are determined using the Canny edge detection algorithm. Next it is checked whether the edges can be combined to form contours, such as object outlines. If there are contours in the frame, their shape is examined. If a contour is recognized as elliptical, it is detected as a possible spatter. This process is also demonstrated in Figure 3.

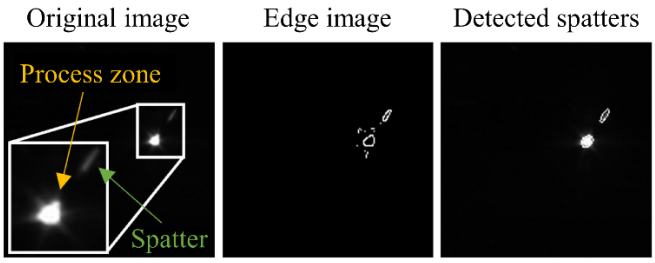

Figure 3: Steps for spatter detection consisting of the original image, edge detection by Canny edge detection algorithm and determination of elliptical contours.

The disparity of the object in the right frame is determined based on the position information of the contour in the left frame. The disparity is then used to determine the 3D position of the spatter. After the spatter detection the spatter tracking can be carried out.
The task of the tracking algorithm is first to determine whether the spatter found has already appeared in one of the previous frames or whether it is a new spatter. For this purpose, various spatter parameters are compared including the frame number, spatter number, flight direction and size of the spatter. The flight direction is approximately calculated as a straight line along the main axis of the ellipse of the respective spatter with which the new one is compared. If the distance between the two spatters is smaller than specified, their direction of flight is compared in the second step. This is done

based on the respective angles as shown in Figure 4. For the general evaluation only spatters that appear in more than one frame are considered.

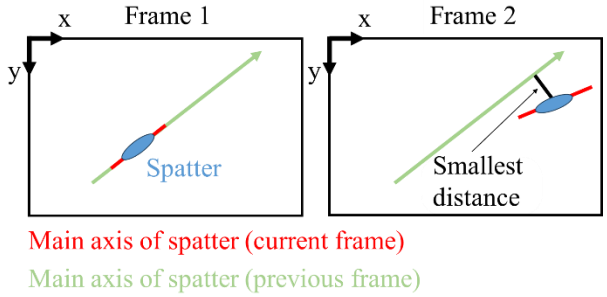

Figure 4: Comparison of spatter flight direction

2.4. Experimental Design

To characterize the spatter behaviour under different processing conditions, a dedicated buildjob was designed. Figure 5 shows the buildjob layout including the gas flow direction (blue), the hatching direction (red) as well as the coordinate system for later evaluation of the camera images.

The buildjob contains four quadratic specimens with a side length of 10 mm of which two are hatched parallel to the gas flow and the other two perpendicular to it. Unidirectional hatching without rotation between the layers was implemented to allow the evaluation of the influence of the gas flow on the spattering. A constant layer thickness of 30 µm and a hatch distance of 100 µm as well as no preheating were used. Before the acquisition of process images, it was made sure that a homogeneous powder bed was established after the first layers. Since no further evaluation of the specimens was planned at this point, the buildjobs were stopped after the acquisition of the images.

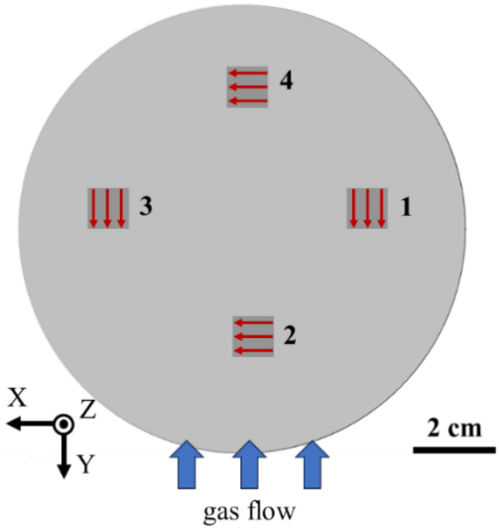

Figure 5: Buildjob layout for spatter characterization with hatching direction marked by red arrows

The buildjob was repeated 3 times with different settings for the parameters laser power P and scanning speed v to realize different volume energy densities (see Table 2). The first buildjob served to investigate the influence of the scanning speed on the spatter behavior while the laser power was kept constant.

The second buildjob was conducted to investigate the influence of the laser powder while keeping the scanning speed constant.

In the third buildjob, the settings for laser power and scanning speed were varied simultaneously. For comparability, the parameter settings were chosen in a way that the volume energy density for the specimens 1 and 2 as well as 3 and 4 for were the same for all buildjobs. This allows for the investigation of the parameter influences at constant volume energy density.

Table 2: Parameter settings

Buildjob	Specimen	Scan direction	Parameter settings	Volume energy density
1	1	Y	P = 200 W, v = 1000 mm/s	66.67 J/mm³
	2	X		
	3	Y	P = 200 W, v = 700 mm/s	95.24 J/mm³
	4	X		
2	1	Y	P = 260 W, v = 1300 mm/s	66.67 J/mm³
	2	X		
	3	Y	P = 372 W, v = 1300 mm/s	95.39 J/mm³
	4	X		
3	1	Y	P = 140 W, v = 700 mm/s	66.67 J/mm³
	2	X		
	3	Y	P = 286 W, v = 1000 mm/s	95.34 J/mm³
	4	X		

3. Results

In the following the results regarding the influence of the gas flow as well as the varied parameters laser power and scanning speed and the resulting volume energy density are presented.

3.1. Influence of gas flow

In a first step, the influence of the gas flow orientation with regard to the scan direction was investigated. Figure 6 shows the observed spatter trajectories for the scanning perpendicular to the gas flow (left) and the scanning parallel to the gas flow (right) for otherwise constant process parameters (P = 200 W, v = 1000 mm/s).
It can be seen that by scanning perpendicular to the gas flow, that the spatter trajectories have a curved shape, confirming the drag out of the process zone by the gas flow. The effects of the of the gas flow are also reflected by the speed of the spatter. The average spatter speed when scanning against the direction of the gas flow is 3.23 m/s. It is therefore higher than when scanning perpendicular to the gas flow where an average spatter speed of 2.78 m/s was determined. This can be explained by the additional acceleration of the spatters by the gas stream that are mainly ejected in the opposite direction of the scanning direction.

3.2. Variation of the scanning speed

The spatter trajectories were evaluated for different scanning speeds. Figure 7 shows the detected trajectories for a scanning speed of 700 mm/s (left) and 1000 mm/s (right).
A significantly higher number of trajectories could be determined for the lower scanning speed (650 trajectories) in comparison to the higher scanning speed (209 trajectories). Furthermore, a difference in spatter size was observed with larger spatters for higher scanning speed (see Table 3). However, no influence on the spatter speed was seen.

Table 3: Spatter properties for constant laser power (200 W)

Direction	v in mm/s	Spatter amount	Mean spatter speed in m/s	Mean spatter size in px
X	1000	203	2.78	15.77
	700	641	3.32	12.13
Y	1000	209	3.22	23.95
	700	650	3.14	18.65

3.3. Variation of the laser power

Figure 8 exemplarily shows the results of the spatter detection for different laser powers (left: 260 W, right: 372 W) at constant scanning speed in Y-direction. Comparing the two graphs reveals that for a higher laser power more spatters can be observed. Additionally, Table 4 shows that the spatters are smaller and have a higher speed for higher laser power. The differences in speed and spatter amount are more pronounced when scanning in X-direction (perpendicular to the gas flow). When scanning parallel to the gas flow also a decrease in spatter size can be observed for increased laser power. When scanning perpendicular to it in X-direction the difference in spatter size is less pronounced.

Table 4: Spatter properties for constant scanning speed (1300 mm/s)

Direction	P in W	Spatter amount	Mean spatter speed in m/s	Mean spatter size in px
X	260	195	3.34	17.77
	372	597	5.01	16.01
Y	260	43	3.67	35.77
	372	197	4.01	25.93

3.4. Investigations at constant volume energy density

In the investigations described before, a variation of the respective process parameter always resulted in a change of the volume energy density and therefore led to a different energy input into the process zone. To investigate the influences of laser power and scanning speed irrespective of the resulting volume energy density, both parameters were varied simultaneously.
Figure 9 shows three process scenarios with the same volume energy density (here E_V = 66,67 Ws/mm³ was chosen exemplarily). The graphs of the determined trajectories are shown in ascending order according to the parameter settings. In a) the parameter combination with the lowest values (P = 140 W, v = 700 mm/s) is shown, followed by b) with the values P = 200 W and v = 1000 mm/s and finally in c) largest with P = 260 W and scanning speed v = 1300 mm/s. The top views on the left of each image show that the number of spatters decreases with increasing values for P and v. Furthermore, the side views on the right show a declining spatter ejection angle for increasing parameter values. Both observations are also confirmed by the determined figures displayed in Table 5. Here it can also be seen that with increasing values for P and v, the spatter speed and spatter size both increase.

Table 5: Spatter properties for constant volume energy density (66.67 J/mm³)

Direct-ion	Parameters	Spatter amount	Mean spatter speed in m/s	Mean spatter size in px
X	P = 140 W v = 700 mm/s E_V = 66.67 J/mm³	379	2.59	13.01
	P = 200 W v = 1000 mm/s E_V = 66.67 J/mm³	203	2.78	15.77
	P = 260 W v = 1300 mm/s E_V = 66.67 J/mm³	195	3.34	17.77
Y	P = 140 W v = 700 mm/s E_V = 66.67 J/mm³	599	2.79	13.18
	P = 200 W v = 1000 mm/s E_V = 66.67 J/mm³	209	3.23	23.95
	P = 260 W v = 1300 mm/s E_V = 66.67 J/mm³	43	3.67	35.77

4. Discussion

The results show that the developed system is able to record and process the spattering with high precision and allows thorough analysis of different spatter properties. However, since the cameras are working in the visible light spectrum, only hot spatter particles can be observed. According to Ly et al., the majority of spatters originates from entrained powder [20]. Not all of these particles are heated up. Consequently, there is an unknown proportion of spatters that cannot be detected with this system. Furthermore, as the particles cool down, they appear smaller on the camera images since less light is emitted from them.

Furthermore, it was noticed in some evaluations that there were some trajectories that deviated from the majority of spatter trajectories. These are classified as possible misdetections of the program that could not be filtered out. Possible causes for the false detections include reflections that were not eliminated or incorrect assignments in the tracking algorithm. However, the number of possible errors is rather low compared to the total number of splashes detected. Based on this, the results are only slightly influenced by the false detections. Nevertheless, future investigations will aim to improve the algorithm.

The detected spatter speeds in this work range from 13.01 m/s to 35,77 m/s and are therefore comparable to the values reported by Ly et al. with 2 – 20 m/s [20]. Nevertheless, it is important to mention that different monitoring setups lead to different results especially regarding the spatter speed since single camera setups lead to a projection of the spatter trajectories onto the viewing plane.

The experimental results show that an isolated variation of laser power and scanning speed leads to similar results regarding the spatter amount and size. A decrease in scanning speed as well as an increase of the laser power both lead to an increase in volume energy density. This results in a higher number of detected spatters and a decreased mean size of these spatters. A higher energy input leads to higher melt pool temperatures and therefore a reduced melt viscosity. It is therefore easier for droplet spatters to escape from the melt pool. Additionally, more particles are entrained from the surrounding powder bed increasing the number of heated particles that also appear as illuminated spatters on the camera images.

However, when investigating process scenarios with constant volume energy density it can be seen, that the spatter behavior cannot be explained solely by this parameter. Instead, the underlying settings as well as the scanning strategy with regard to the gas flow need to be taken into account. It was demonstrated that an increase of both, laser power and scanning speed at constant E_V led to less and larger spatters. This supports the results of Andani et al. that show that the scanning speed has a greater influence than the laser power [14]. The higher the scanning speed the higher the cooling rate of the melt pool. Furthermore, the scanning speed influences the inclination angle of the front and back wall of the keyhole and therefore the spatter angle as demonstrated by the presented spatter trajectories in Figure 9. With increasing scanning speed, the keyhole is wider and less deep [11,21]. This results in a more backward orientated spatter ejection compared to an upward ejection for low scanning speed. The higher spatter speed, amount and size when scanning in Y-direction (parallel to the gas flow) can be attributed to the penetration of the melt pool by the gas flow as well as the additional acceleration of the spatters. The majority of spatters flies in the opposite direction of the scanning direction. Thus, in the case of scanning in Y-direction the spatter trajectories already coincide with the gas flow direction and gain more speed. The penetration of the melt pool by the gas flow is promoted when scanning in this direction. It induces melt pool instabilities and therefore causes increased spatter generation. To reduce the spattering and improve process stability and part quality it is therefore

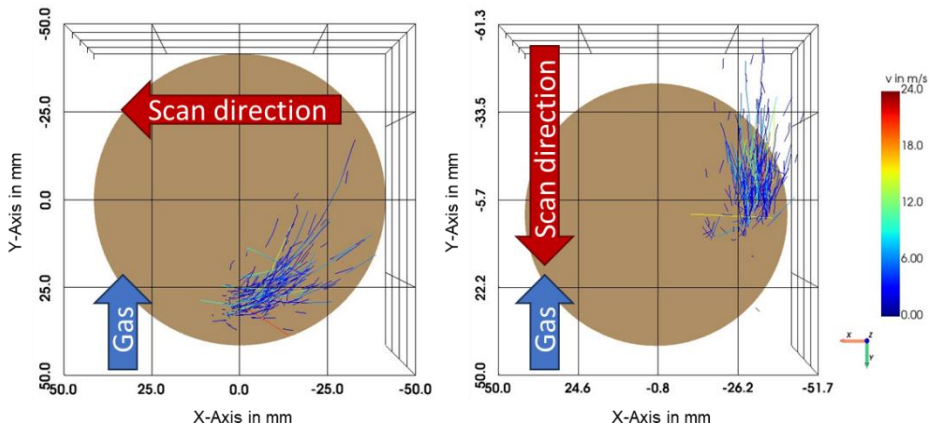

Figure 8: Spatter trajectories for different scan directions with regard to the gas flow direction (P = 200 W, v = 1000 mm/s)

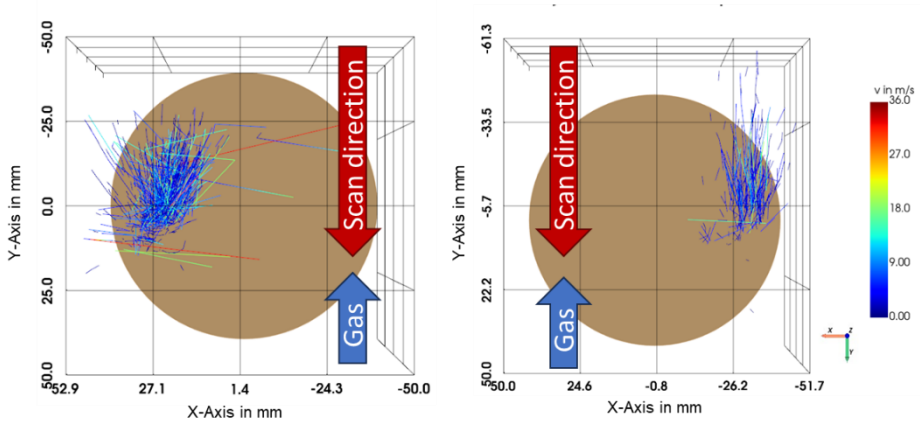

Figure 6: Spatter trajectories for constant laser power of 200 W (left: v = 700 mm/s, right: v = 1000 mm/s)

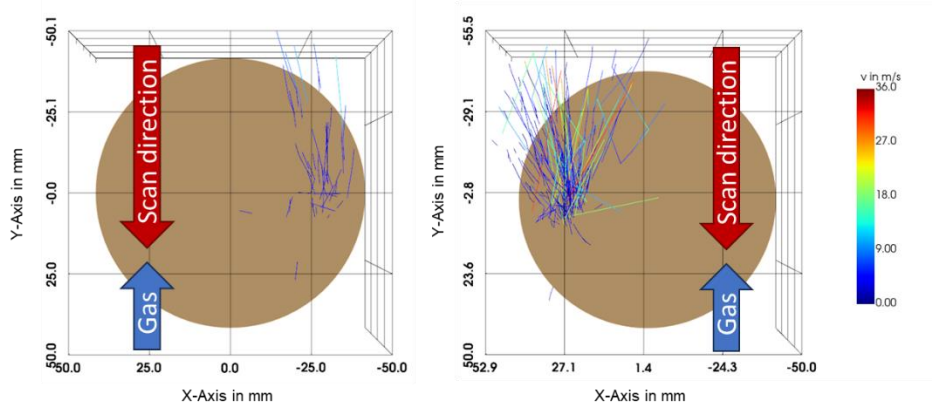

Figure 7: Spatter trajectories for constant scanning speed of 1300 mm/s (left: P = 260 W, right: P = 372 W)

recommended to primarily adjust the scanning speed and then adjust the laser power based on additional quality parameters like porosity and roughness. Scanning parallel to the gas flow is highly disadvantageous and should be avoided.

It is important to mention, that the presented results were obtained through the conduction of single buildjobs. They serve to give a first impression of the underlying mechanisms of spatter generation and to demonstrate the feasibility of the developed stereo system. For statistically secured statements, it is necessary to conduct a higher number of buildjobs and a broader range of parameter settings in future studies.

Regarding the industrial applicability the demonstrated system represents a highly useful and easily integrable solution that could also be used in commercial machines. Since only two USB connections are needed, not much wiring is required. The developed programs for evaluations could supplement existing commercial tools like melt pool monitoring.

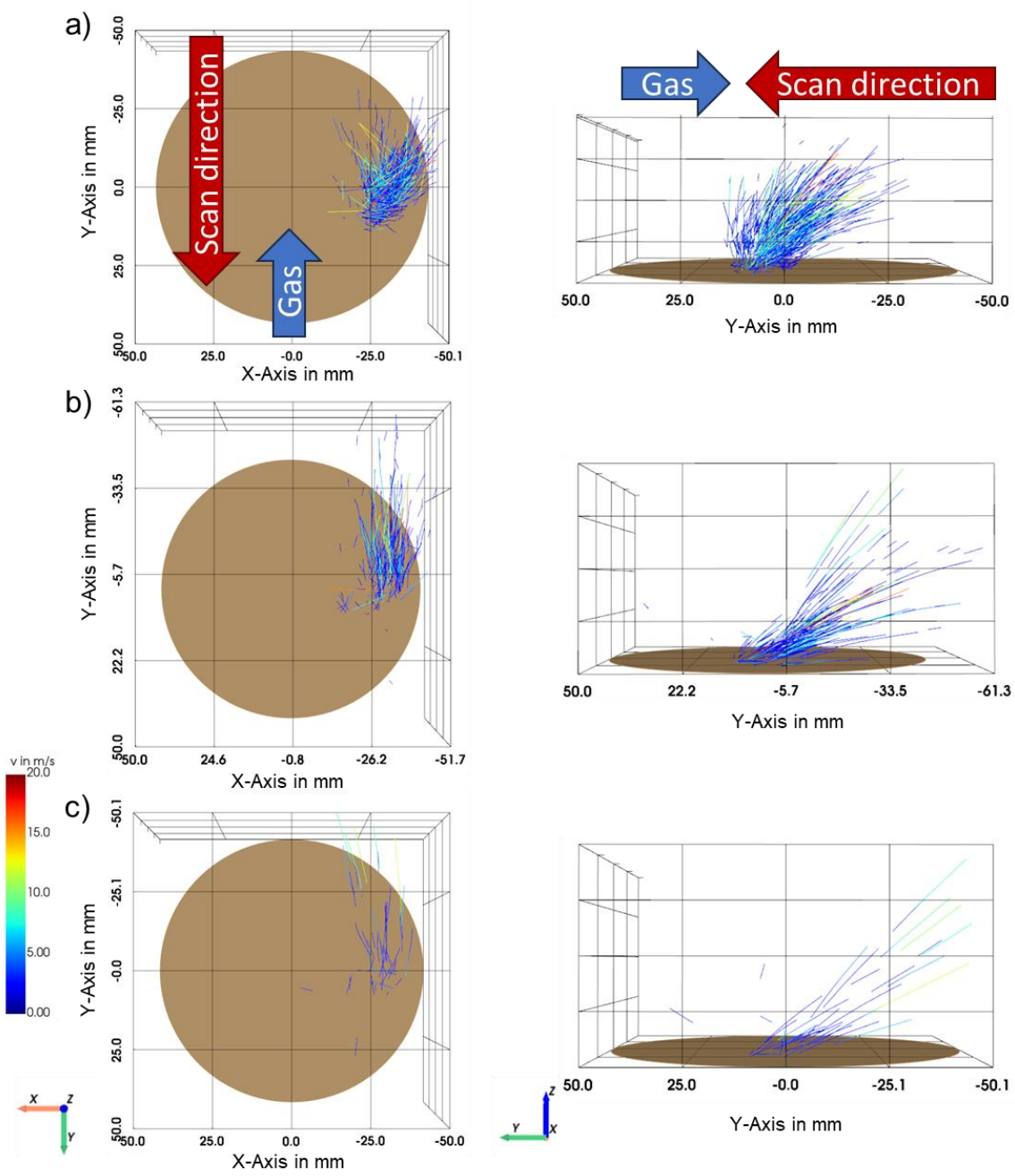

Figure 9: Top and side views of the spatter trajectories for constant volume energy density of 66.67 J/mm³ and different parameter settings: a) P = 140 W, v = 700 mm/s, b) P = 200 W, v = 1000 mm/s, c) P = 260 W, v = 1300 mm/s

5. Conclusion and outlook

In this work, a stereo-camera system was set up and programs for spatter detection and tracking in the three-dimensional space were developed. These programs were then used to investigate the influence of the gas flow as well as the process parameters and the resulting volume energy density on the spatter behavior.
The following conclusions can be given:

- Using two low-cost, small-sized high-speed cameras with a framerate of 500 fps and implementing a python algorithm using OpenCV and the Canny edge detection algorithm enables the three-dimensional tracking and characterization of spatters.
- The gas flow strongly influences the spatter trajectories. A perpendicular orientation of gas flow and scanning direction results in curved trajectories. When gas flow and scanning direction coincide, higher spatter speeds, spatter amounts and sizes can be observed.

- The spatter characteristics are influenced by the volume energy density and the underlying parameters scanning speed and laser power. The scanning speed has a stronger influence. For increasing values, a decreasing spatter angle could be observed.

This work shows the importance of not only optimizing the volume energy density for reducing the spattering but also to adjust the underlying parameters and the orientation towards the gas flow. Future investigations will provide deeper insights into the influence of the gas flow speed as well as the correlation of the spatter characteristics and part properties including porosity and roughness.

6. Acknowledgement

The research project “Vertical E2E – Vertically integrated, sustainable end-to-end factory” was funded by NBank as part of the Lower Saxony aviation funding guidelines and was supervised by the German Aerospace Center (DLR) as project sponsor. The authors would like to express their sincere thanks to the sponsors for their financial support in this project.

7. Contributions

Nicole Emminghaus: writing – original draft preparation, interpretation, visualization
Tim Klügel: conceptualization, executive trials, interpretation, visualization, software development
Jörg Hermsdorf: writing – review and editing, supervision
Stefan Kaierle: writing – review and editing, supervision

References

[1] P. Edwards, M. Ramulu, Fatigue performance evaluation of selective laser melted Ti–6Al–4V, Materials Science and Engineering: A 598 (2014) 327–337. https://doi.org/10.1016/j.msea.2014.01.041.

[2] K. Gruber, I. Smolina, M. Kasprowicz, T. Kurzynowski, Evaluation of Inconel 718 Metallic Powder to Optimize the Reuse of Powder and to Improve the Performance and Sustainability of the Laser Powder Bed Fusion (LPBF) Process, Materials 14 (2021) 1538. https://doi.org/10.3390/ma14061538.

[3] N. Derimow, N. Hrabe, Oxidation in Reused Powder Bed Fusion Additive Manufacturing Ti-6Al-4V Feedstock: A Brief Review, JOM 73 (2021) 3618–3638. https://doi.org/10.1007/s11837-021-04872-y.

[4] S. Vock, B. Klöden, A. Kirchner, T. Weißgärber, B. Kieback, Powders for powder bed fusion: a review, Prog Addit Manuf 4 (2019) 383–397. https://doi.org/10.1007/s40964-019-00078-6.

[5] A. Raza, T. Fiegl, I. Hanif, A. Markström, M. Franke, C. Körner, E. Hryha, Degradation of AlSi10Mg powder during laser based powder bed fusion processing, Materials & Design 198 (2021) 109358. https://doi.org/10.1016/j.matdes.2020.109358.

[6] A. Raza, C. Pauzon, E. Hryha, A. Markström, P. Forêt, Spatter oxidation during laser powder bed fusion of Alloy 718: Dependence on oxygen content in the process atmosphere, Additive Manufacturing 48 (2021) 102369. https://doi.org/10.1016/j.addma.2021.102369.

[7] R. Williams, M. Bilton, N. Harrison, P. Fox, The impact of oxidised powder particles on the microstructure and mechanical properties of Ti-6Al-4 V processed by laser powder bed fusion, Additive Manufacturing 46 (2021) 102181. https://doi.org/10.1016/j.addma.2021.102181.

[8] S. Pal, G. Lojen, R. Hudak, V. Rajtukova, T. Brajlih, V. Kokol, I. Drstvenšek, As-fabricated surface morphologies of Ti-6Al-4V samples fabricated by different laser processing parameters in selective laser melting, Additive Manufacturing 33 (2020) 101147. https://doi.org/10.1016/j.addma.2020.101147.

[9] U. Ali, R. Esmaeilizadeh, F. Ahmed, D. Sarker, W. Muhammad, A. Keshavarzkermani, Y. Mahmoodkhani, E. Marzbanrad, E. Toyserkani, Identification and characterization of spatter particles and their effect on surface roughness, density and mechanical response of 17-4 PH stainless steel laser powder-bed fusion parts, Materials Science and Engineering: A 756 (2019) 98–107. https://doi.org/10.1016/j.msea.2019.04.026.

[10] Z. Li, H. Li, J. Yin, Y. Li, Z. Nie, X. Li, D. You, K. Guan, W. Duan, L. Cao, D. Wang, L. Ke, Y. Liu, P. Zhao, L. Wang, K. Zhu, Z. Zhang, L. Gao, L. Hao, A Review of Spatter in Laser Powder Bed Fusion Additive Manufacturing: In Situ Detection, Generation, Effects, and Countermeasures, Micromachines 13 (2022) 1366. https://doi.org/10.3390/mi13081366.

[11] Di Wang, W. Dou, Y. Ou, Y. Yang, C. Tan, Y. Zhang, Characteristics of droplet spatter

behavior and process-correlated mapping model in laser powder bed fusion, Journal of Materials Research and Technology 12 (2021) 1051–1064. https://doi.org/10.1016/j.jmrt.2021.02.043.

[12] D. Yang, H. Li, S. Liu, C. Song, Y. Yang, S. Shen, J. Lu, Z. Liu, Y. Zhu, In situ capture of spatter signature of SLM process using maximum entropy double threshold image processing method based on genetic algorithm, Optics & Laser Technology 131 (2020) 106371. https://doi.org/10.1016/j.optlastec.2020.106371.

[13] D. Ye, J.Y. Hsi Fuh, Y. Zhang, G.S. Hong, K. Zhu, In situ monitoring of selective laser melting using plume and spatter signatures by deep belief networks, ISA Transactions 81 (2018) 96–104. https://doi.org/10.1016/j.isatra.2018.07.021.

[14] M.T. Andani, R. Dehghani, M.R. Karamooz-Ravari, R. Mirzaeifar, J. Ni, A study on the effect of energy input on spatter particles creation during selective laser melting process, Additive Manufacturing 20 (2018) 33–43. https://doi.org/10.1016/j.addma.2017.12.009.

[15] Y. Zhang, H.G. Soon, D. Ye, J.Y.H. Fuh, K. Zhu, Powder-Bed Fusion Process Monitoring by Machine Vision With Hybrid Convolutional Neural Networks, IEEE Trans. Ind. Inf. 16 (2020) 5769–5779. https://doi.org/10.1109/tii.2019.2956078.

[16] H. Zheng, H. Li, L. Lang, S. Gong, Y. Ge, Effects of scan speed on vapor plume behavior and spatter generation in laser powder bed fusion additive manufacturing, Journal of Manufacturing Processes 36 (2018) 60–67. https://doi.org/10.1016/j.jmapro.2018.09.011.

[17] C. Barrett, C. Carradero, E. Harris, J. McKnight, J. Walker, E. MacDonald, B. Conner, Low cost, high speed stereovision for spatter tracking in laser powder bed fusion, 2018 International Solid Freeform Fabrication Symposium. University of Texas at Austin (2018).

[18] E. Eschner, T. Staudt, M. Schmidt, Sensing approach for the in-situ determination of spatter motion within PBF-LB/M, CIRP Annals 71 (2022) 149–152. https://doi.org/10.1016/j.cirp.2022.03.005.

[19] N. Emminghaus, S. Fritsch, H. Büttner, J. August, M. Tegtmeier, M. Huse, M. Lammers, C. Hoff, J. Hermsdorf, S. Kaierle, PBF-LB/M process under a silane-doped argon atmosphere: Preliminary studies and development of an innovative machine concept, Advances in Industrial and Manufacturing Engineering 2 (2021) 100040. https://doi.org/10.1016/j.aime.2021.100040.

[20] S. Ly, A.M. Rubenchik, S.A. Khairallah, G. Guss, M.J. Matthews, Metal vapor micro-jet controls material redistribution in laser powder bed fusion additive manufacturing, Sci Rep 7 (2017) 4085. https://doi.org/10.1038/s41598-017-04237-z.

[21] W.E. King, H.D. Barth, V.M. Castillo, G.F. Gallegos, J.W. Gibbs, D.E. Hahn, C. Kamath, A.M. Rubenchik, Observation of keyhole-mode laser melting in laser powder-bed fusion additive manufacturing, Journal of Materials Processing Technology 214 (2014) 2915–2925. https://doi.org/10.1016/j.jmatprotec.2014.06.005.